Nature Communications

https://doi.org/10.1038/s41467-026-73864-w

Article in Press

Secretin-interacting plug proteins prevent antibiotic influx during type IV pilus assembly in *Pseudomonas aeruginosa*

Received: 29 March 2026

Accepted: 19 May 2026

Cite this article as: Kwon, O.H., Lee, Y., Ryu, B. *et al.* Secretin-interacting plug proteins prevent antibiotic influx during type IV pilus assembly in *Pseudomonas aeruginosa*. *Nat Commun* (2026). https://doi.org/10.1038/s41467-026-73864-w

Oh Hyun Kwon, Yeseul Lee, Bumhan Ryu, Joel W. Sher, Sohee Park, Frédéric Lauber, Bi-o Kim, Youngki Yoo, Seung-Hyun Cho, Donghui Choe, You-Hee Cho, Jean-François Collet, Melanie D. Ohi, Thomas G. Bernhardt, Jeong Min Chung & Hongbaek Cho

Secretin-interacting plug proteins prevent antibiotic influx during type IV pilus assembly in *Pseudomonas aeruginosa*.

Oh Hyun Kwon[1,2†], Yeseul Lee[2†], Bumhan Ryu[3†], Joel W Sher[4], Sohee Park[1], Frédéric Lauber[5,6], Bi-o Kim[1], Youngki Yoo[7], Seung-Hyun Cho[5,6], Donghui Choe[1], You-Hee Cho[8], Jean-François Collet[5,6], Melanie D Ohi[7,9], Thomas G Bernhardt[4,10], Jeong Min Chung[2*], and Hongbaek Cho[1*]

[†]contributed equally

[1]Department of Biological Sciences, College of Natural Sciences, Sungkyunkwan University, Suwon 16419, Republic of Korea

[2]Department of Biotechnology, The Catholic University of Korea, Bucheon 14662, Republic of Korea

[3]Research Solution Center, Institute for Basic Science, Daejeon 34126, Republic of Korea

[4]Department of Microbiology, Blavatnik Institute, Harvard Medical School, Boston, MA, USA

[5]WELBIO Department, WEL Research Institute, Avenue Pasteur, 6, 1300 Wavre, Belgium

[6]de Duve Institute, Université catholique de Louvain (UCLouvain), Avenue Hippocrate 75, 1200 Brussels, Belgium

[7]Life Sciences Institute, University of Michigan, Ann Arbor, Michigan, USA.

[8]Department of Pharmacy, College of Pharmacy and Institute of Pharmaceutical Sciences CHA University, Republic of Korea

[9]Department of Cell and Developmental Biology, University of Michigan, Ann Arbor, Michigan, USA.

[10]Howard Hughes Medical Institute, Harvard Medical School, Boston, MA, USA

*To whom correspondence should be addressed.

Hongbaek Cho, Ph.D.

Sungkyunkwan University

Department of Biological Sciences

Suwon 16419, Republic of Korea

e-mail: hongbaek@skku.edu

Jeong Min Chung, Ph.D.

The Catholic University of Korea

Department of Biotechnology

Bucheon 14662, Republic of Korea

e-mail: jmchung@catholic.ac.kr

Key words: type IV pili, secretin, plug, outer membrane, permeability barrier, antibiotics, drug resistance

Abstract

Type IV pili (T4P) are important virulence factors that mediate host attachment and other pathogenic functions. In Gram-negative bacteria, T4P are assembled from pilin subunits at the inner membrane (IM) and extend through the outer membrane (OM) via secretin channels. Although essential for T4P function, secretin complexes can impair the OM permeability barrier, potentially allowing entry of toxic compounds. The mechanisms that prevent such influx remain poorly understood. Here, we identify SlkA and SlkB (PA5122 and PA5123) as periplasmic proteins that interact with the T4P secretin channel and block antibiotic influx. Our data indicate that these proteins function as physical plugs sealing the channel until the IM complex docks and pilus assembly begins. These findings demonstrate that Slk proteins and the IM complex function redundantly to maintain OM barrier integrity, and that their interaction with the secretin channel represents a promising target for antibiotic potentiation.

Key words: type IV pili, secretin channel, plug, outer membrane, permeability barrier, antibiotics, drug resistance

Introduction

The cell envelope of Gram-negative bacterial pathogens plays a major role in developing multidrug resistance by functioning as an effective barrier against antibiotics[1,2]. In particular, the outer membrane (OM) effectively restricts the diffusion of various toxic compounds. In addition, resistance-nodulation-division (RND) family efflux pumps spanning the envelope efficiently expel toxic molecules, further reinforcing the barrier function[3–6]. However, the OM barrier is inherently imperfect, as it must also support essential molecular transport, including nutrient uptake and the secretion of virulence factors. General porins and substrate-specific channels, which facilitate the diffusion of small hydrophilic nutrients, can serve as entry points for hydrophilic antibiotics[7,8]. In addition to porins, Gram-negative pathogens assemble multimeric OM channels as part of transenvelope complexes such as pili and secretion systems, most of which are critical for virulence and survival in the host[1].

A group of homologous proteins called secretins form 12- to 15-meric OM channel complexes to accommodate protein substrates in several envelope-spanning virulence systems: type II secretion systems (T2SS), type III secretion systems (T3SS), and type IV pili assembly systems (T4PS)[9,10]. Cryo-electron microscopy (cryo-EM) of the secretin complexes revealed a conserved architecture consisting of an N-terminal periplasmic vestibule that interacts with the inner membrane (IM) components of the virulence system and a C-terminal OM channel with one or two gate structures[11–14]. Although secretin channels form much larger pore structures than the porins, it has been assumed that their gate structures prevent leakage of periplasmic contents and influx of extracellular chemicals when they are not in use for protein secretion or pilus assembly[9,10]. However, *in vitro* studies suggest that secretin channels are not completely sealed in their resting state and that permeation of small compounds occurs through these channels[15], but the mechanisms preventing leakage remain unclear.

In this study, we identified and characterized two genes, *slkA* and *slkB* (formerly *PA5122* and *PA5123*), that prevent secretin leakiness in *P. aeruginosa*. Genetic and microscopic analyses suggested that Slk proteins prevent drug diffusion through the OM secretin channels of the T4PS when these channels are not docked with the IM complex. Cryo-EM imaging of secretin channels from strains with or without *slk* expression revealed that Slk proteins interact with the channel's gate structure, supporting their role as physical plugs. Overall, our findings demonstrate that the gate structure of secretin channels alone is insufficient to maintain the OM permeability barrier and that dedicated plug proteins prevent the entry of toxic compounds during vulnerable stages of T4P assembly, particularly when IM complex assembly is delayed or misaligned with the OM secretin channel.

Results

SlkA and SlkB are periplasmic proteins important for maintaining the OM barrier

To identify factors contributing to OM barrier function in *P. aeruginosa*, we performed transposon sequencing (Tn-seq) analysis of strain PAO1 following exposure to erythromycin, a hydrophobic antibiotic that normally does not inhibit growth due to the barrier function of the OM (Fig. 1a). Comparison of transposon insertion profiles between erythromycin-treated and untreated samples revealed a marked reduction of insertions in *oprM* and *PA5122* upon drug exposure, suggesting these genes play important roles for survival in the presence of erythromycin (Fig. 1b). Since *oprM* encodes the OM channel component of major RND efflux systems MexAB-OprM and MexXY-OprM[6,16,17], the *oprM* mutant is likely to be hypersensitive to erythromycin due to defective efflux activity. In contrast, the function of *PA5122* was uncharacterized, so we focused on elucidating its cellular function.

PA5122 is predicted to encode a periplasmic protein, suggesting a role in maintaining the envelope barrier rather than directly blocking erythromycin's action on the ribosome. *PA5122* appears to form an operon with the downstream homolog *PA5123* (Fig. 1b and Supplementary Fig. 1), but only disruption of *PA5122* caused erythromycin susceptibility, consistent with the Tn-seq results (Fig. 1c). We hypothesized that PA5122 and PA5123 are functionally redundant, and that either PA5123 is poorly expressed under lab growth conditions or *PA5122* mutation causes erythromycin sensitivity through a polar effect that reduces *PA5123* expression as well. Indeed, *PA5123* transcript levels were significantly lower in the *PA5122* mutant than in the WT strain (Supplementary Fig. 2). To test whether PA5122 and PA5123 have similar functions, each gene was expressed individually in the *ΔPA5122-PA5123* strain. Expression of either gene restored resistance (Fig. 1d), indicating that PA5122 and PA5123 function redundantly. Based on our findings presented below, we discovered that PA5122 and PA5123 prevent compound influx

through the T4P secretin channel and will henceforth refer to them as SlkA and SlkB for prevention of secretin leakiness.

To test if inactivation of Slk proteins causes a general defect in envelope barrier function, we examined the *ΔslkAB* strain for sensitivity to various antibiotics. The *slkAB* mutation increased sensitivity to macrolides (erythromycin and azithromycin), aminoglycosides (gentamicin and tobramycin), and trimethoprim-sulfamethoxazole (TMP-SMX) (Fig. 1e and Supplementary Fig. 3). These antibiotic sensitivity profiles differed from those of the *ΔoprM* strain: the *ΔslkAB* strain was more susceptible to macrolides, whereas the *ΔoprM* strain was more sensitive to aminoglycosides and TMP-SMX, suggesting that Slk proteins likely function independently of the MexAB-OprM and MexXY-OprM efflux pumps.

Slk proteins prevent antibiotic influx through the T4P OM secretin channel

To investigate the cellular function of Slk proteins, we performed a genetic selection for suppressors of erythromycin sensitivity in the *ΔslkAB* strain using transposon mutagenesis (Fig. 2a). Most suppressor mutations mapped to *pilQ*, which encodes the secretin forming the OM channel of *P. aeruginosa* T4P. Other mutations mapped to genes upstream of *pilQ*, which were previously reported to significantly lower PilQ protein levels[18], or to genes required for secretin channel assembly, *pilF* and *fimV*[19,20]. Thus, assembly of the T4P secretin channel in the absence of Slk proteins seemed responsible for the antibiotic sensitivity of the *ΔslkAB* strain. Indeed, erythromycin sensitivity of the *ΔslkAB* strain was suppressed by a *pilQ* null mutation and restored by ectopic *pilQ* expression (Fig. 2b). Moreover, *pilQ* expression alone was sufficient to reverse the suppression conferred by *ΔpilMNOPQ*, indicating that mutations upstream of *pilQ* suppress the sensitivity via a polar effect on *pilQ* expression. Although a *pilQ* mutation suppressed the *ΔslkAB* antibiotic sensitivity phenotype, it did not increase resistance in

the wild-type strain (Fig. 2c), indicating that secretin channel assembly does not compromise envelope barrier when the *slkAB* genes are expressed normally.

Defective IM complex assembly leads to antibiotic influx through the secretin channel in the absence of Slk proteins

Because we found that Slk proteins are functionally linked to T4P, we tested if they are required for twitching motility. Unexpectedly, the PAO1 strain used for the Tn-seq analysis and initial mutant characterization was defective in twitching motility (Fig. 3a). Genetic variability among PAO1 strains is widely recognized[21–23]. We therefore obtained a twitching-proficient PAO1 strain (PAO1^{tw+}) and other *P. aeruginosa* strains, PA14 and PAK, to assess twitching phenotypes. In these strains, *ΔslkAB* did not cause an obvious defect in twitching motility, showing that Slk proteins are not essential components of T4P (Fig. 3a). Surprisingly, however, *ΔslkAB* did not cause obvious erythromycin sensitivity in the twitching-proficient strains, unlike in the twitching-defective PAO1 strain (Fig. 3d and Supplementary Fig. 4). This unexpected result suggested that the erythromycin sensitivity of the *ΔslkAB* mutants in our original strain background is related to its twitching motility defect.

Genome resequencing of the twitching-defective PAO1 strain revealed a frameshift mutation in *pilC* (Supplementary Fig. 5 and Supplementary Data 1-2), which encodes the platform protein that coordinates T4P polymerization and depolymerization[24]. Ectopic expression of *pilC* restored twitching motility in the defective PAO1 strain and its *ΔslkAB* derivative (Fig. 3b). Notably, it also restored erythromycin resistance to the *ΔslkAB* strain (Fig. 3c), indicating that both *pilC* and *slkAB* mutations are required to cause erythromycin sensitivity. Moreover, combining *pilC* and *slkAB* deletions in twitching-proficient strains resulted in erythromycin sensitivity, which was again suppressed by a *pilQ* mutation (Fig. 3d and Supplementary Fig. 4). These results

suggested that the PilQ secretin channel functions as a conduit for antibiotic influx when Slk proteins are inactivated and T4P assembly is disrupted by loss of PilC.

We next sought to determine if other mutations that cause a defect in T4P assembly also result in antibiotic permeation through the PilQ channel in the *ΔslkAB* strain. The T4P assembly system is composed of four subcomplexes: (i) the platform protein PilC and cytoplasmic motor proteins PilBTU; (ii) the pilus shaft consisting of the major pilin PilA, minor pilins FimU-PilVWXE, and the adhesin PilY1; (iii) the alignment complex made up of PilMNOP; and (iv) the secretin complex consisting of PilQ and TsaP [25,26]. We reasoned that loss of the pilus shaft leaves the PilQ secretin pore unoccupied, allowing antibiotic permeation through the pore in the absence of Slk proteins. Consistent with this idea, deletion of the major pilin *pilA* or the adhesin *pilY1* caused erythromycin sensitivity in the *ΔslkAB* derivative of the PAO1^{tw+} strain, and the sensitivity was suppressed by *pilQ* deletion as observed for *pilC* mutants (Fig. 3e).

To test the effect of mutations in genes encoding the alignment complex on antibiotic influx through the PilQ channel, we used a *ΔpilMNOPQ* mutant strain expressing *pilQ* from an inducible promoter to account for the polarity of *pilMNOP* mutations on downstream *pilQ* expression[18] (Fig. 2b). The *ΔslkAB ΔpilMNOPQ* mutant strain became erythromycin-sensitive upon *pilQ* induction but remained resistant without ectopic *pilQ* expression (Fig. 3f). These results indicate that, in the absence of Slk proteins, disruption of T4P subcomplexes at the IM generally leads to a PilQ-mediated defect in the OM permeation barrier.

To further assess the contributions of Slk proteins and the IM complex to preventing toxic molecule influx through PilQ, we compared the erythromycin sensitivity of the *ΔslkAB*, *ΔpilC*, *ΔpilQ*, and WT strains using MIC assays (Supplementary Fig. 6). The *ΔslkAB* mutant showed increased sensitivity at a concentration twofold below the MIC, although the increase was not as dramatic as that observed in the *ΔslkAB ΔpilC* mutant. Importantly, the increased sensitivity of

the *ΔslkAB* mutant was also suppressed by *ΔpilQ*, indicating that it results from increased influx through PilQ. In contrast, the *ΔpilC* mutant displayed sensitivity similar to that of the WT or *ΔpilQ* strain, indicating that defective IM complex assembly alone does not increase influx through PilQ. The finding that PilQ-dependent sensitivity increases in the *ΔslkAB* mutant, but not in the *ΔpilC* mutant when Slk proteins are present, indicates that Slk proteins play a primary role in preventing toxic molecule influx through PilQ.

Slk proteins interact with the PilQ secretin complex

The above results led us to hypothesize that Slk proteins prevent antibiotic influx by interacting with the PilQ secretin channel when the channel is not docked with the IM complex. As PilQ localizes to the poles independently of Slk proteins or the IM complex assembly (Supplementary Fig. 7)[27], we reasoned that the interaction between Slk proteins and the PilQ channel can be assessed by examining the polar localization of Slk proteins using fluorescent protein fusions in the PAO1^{tw+} strain and its T4P mutant derivatives. Consistent with our hypothesis, SlkA-mScarlet and SlkB-mScarlet localized to the poles in a PilQ-dependent fashion, albeit weakly, indicating that Slk proteins interact with the PilQ secretin complex (Fig. 4 and Supplementary Fig. 8). Notably, polar localization of Slk proteins was enhanced when IM complex assembly was impaired by a *ΔpilC* mutation, indicating that Slk proteins interact more strongly with the PilQ channel when the IM complex assembly is inhibited. These results imply that Slk proteins and the IM complex compete for interaction with the PilQ channel and that Slk proteins are displaced when the IM complex docks with the channel. Overall, the localization patterns of Slk proteins in wild-type and T4P mutant strains are consistent with our hypothesis that Slk proteins interact with the PilQ channel to prevent antibiotic influx through the channel when it is not properly assembled with the IM complex.

Slk proteins occlude the PilQ channel near its gate

To understand how Slk proteins interact with the PilQ channel to prevent compound influx, we determined single-particle cryo-EM structures of PilQ prepared from strains expressing *slkA*, *slkB*, or neither. These strains also carried a *pilC* deletion, introduced to disrupt IM complex assembly and thereby enhance PilQ-Slk binding. Reconstructions of PilQ from strains expressing *slkA* or *slkB* revealed density continuous with the gate and occupying the central lumen from the vestibule toward the periplasm, whereas PilQ prepared without *slk* expression showed an unobstructed conduit (Fig. 5a and Supplementary Fig. 11a,12), suggesting the luminal mass corresponds to Slk proteins. The luminal mass sits deeper and contacts a broader region of the inner wall in PilQ when *slkB* is expressed than when SlkA is produced, indicating that these densities represent related but distinct proteins, consistent with their assignment as SlkA or SlkB. Label-free proteomics of the same preparations detected SlkA exclusively in PilQ–*slkA* samples and SlkB exclusively in PilQ–*slkB* samples, with neither paralogue detected in PilQ-only controls (Supplementary Table 1), supporting the assignment of the luminal density to Slk proteins. Local-resolution estimates and asymmetric C1 reconstructions are consistent with this assignment (Supplementary Fig. 13). The PilQ channel is well resolved and relatively uniform in local resolution. By contrast, the luminal mass is lower in local resolution and shows small class-to-class positional variability, which we interpret as mild positional heterogeneity consistent with a restrained but mobile plug. To directly assess heterogeneity, we performed 3D variability analysis (3DVA) in C1 using a lumen-restricted mask; the principal modes revealed motions confined to the luminal density with minimal deformation of the surrounding barrel (Supplementary Movies 1–6). Taken together, our structural and proteomic analyses suggest that Slk proteins interact with the PilQ channel at the gate and function as a plug, providing

barrier function beyond that of the gate alone.

Slk-bound PilQ likely represents an in situ pre-docking stage of T4P secretin channels

Cryo-ET studies of T4PS in *Myxococcus xanthus* and *P. aeruginosa* have shown that in strains with impaired pilus assembly, such as *ΔpilC* or *ΔpilY1*, PilQ secretin channels remain undocked due to defective IM complex assembly[28–30]. These secretin channels likely correspond to the pre-docking stage of the T4PS prior to IM complex engagement in cells. To test whether the *in vitro* Slk-bound state reflects this stage, we performed rigid alignment of PilQ–SlkA and PilQ–SlkB maps to subtomogram averages of the T4P system in the *P. aeruginosa pilY1* mutant [EMD-43432][30]. This alignment placed the Slk mass at the site of the central luminal density observed *in situ* (Fig. 5b,c and Supplementary Fig. 11). Notably, this density is absent in tomograms of *M. xanthus pilC* or *pilY1* mutants[28,29], which lack *slk* homologs (Supplementary Fig. 14), suggesting that the central luminal density in the *P. aeruginosa pilY1* mutant likely represents Slk proteins. Consistent with this interpretation, label-free TIMS-TOF proteomics did not detect minor pilins (FimU, PilV/W/X/E) or PilY1 in PilQ-only or PilQ–*slkB* samples. In PilQ–*slkA* samples, PilV and PilY1 were detected only at trace levels relative to PilQ and SlkA (Supplementary Table 1), likely reflecting low-level carryover or non-stoichiometric co-purification, below the threshold for confident assignment. Together with the spatial overlap between the *in situ* gate-proximal T-shaped density and our Slk mass, these data support assigning the central luminal density to Slk proteins rather than to the minor-pilin/PilY1 complex. Thus, combined with genetic data indicating redundant functions of Slk proteins and the IM complex in preventing influx through the PilQ secretin channel (Fig. 3,4), our structural analysis suggests that during T4PS assembly in *P. aeruginosa*, Slk proteins act as an initial plug within the PilQ lumen until the IM complex docks to the secretin channel and pilus assembly proceeds.

Discussion

The OM of Gram-negative bacteria serves as an effective permeability barrier against antibiotics. However, channel structures in the OM, which carry out critical functions for survival and virulence, can compromise this barrier. Secretin complexes, assembled as OM channels of important transenvelope virulence systems such as T4PS and T2SS, represent a class of OM channels that can potentially serve as conduits for drug diffusion. Although these channels have gate structures, *in vitro* evidence suggests that the gates cannot seal the channels completely to prevent compound permeation[15]. In this regard, it has been suggested that the pilus or pseudopilus structures occlude the pores upon docking of the IM complex with the OM secretin channel, and that adhesins such as PilY1 function as plugs in the fully assembled T4PS[29,30]. Nevertheless, because secretin channels assemble independently of the IM complexes, compound permeation could occur at the pre-docking stage, but the mechanism maintaining the OM barrier at this stage has remained unclear.

In this study, we found that mutations impairing IM complex assembly of the T4PS did not compromise the OM permeability barrier in *P. aeruginosa*, apparently contradicting the idea that the IM complex plugs the OM secretin channel to prevent compound influx. Instead, we identified periplasmic proteins, which we renamed Slk proteins, that play a primary role in preventing toxic molecule influx through the PilQ channel after its assembly. We also discovered that impaired IM complex assembly caused a severe synthetic defect in OM barrier function when combined with *slk* mutations, and that this defect was suppressed by a *pilQ* mutation. These findings indicate that, although Slk proteins are the primary factors preventing influx through the PilQ channel, the IM complex also contributes redundantly to this function, revealing a new mechanism for maintaining the OM barrier while reconciling our observations with the prevailing model. Furthermore, cryo-EM analysis of PilQ prepared with or without *slk* expression

demonstrated that Slk proteins localize within the lumen of the PilQ channel and plug the gate structure. Overall, these results reveal that Slk proteins function as plugs that prevent toxic compound entry through the T4P secretin channel, providing a mechanism by which *P. aeruginosa* maintains OM barrier integrity before the T4P IM complex docks with the OM secretin channel or when IM complex assembly is defective (Fig. 5d).

In our assay for Slk-PilQ interaction, using PilQ-dependent polar localization as a proxy, we observed that the interaction was strongly enhanced in the *pilC* mutant defective in IM complex assembly (Fig. 4 and Supplementary Fig. 8). This suggests that Slk proteins interact with the PilQ channel but are displaced when the IM complex engages the channel. Cryo-EM analysis shows that the Slk-derived luminal density resolves at lower local resolution than the PilQ barrel (Supplementary Fig. 13). Consistent with this, 3D variability analysis revealed motions confined to the luminal density (Slk) with minimal deformation of the barrel (PilQ) (Supplementary Movies 1–6). These features support a restrained, mobile engagement rather than a locked insertion, consistent with the role of a plug that is displaced upon full T4P assembly. A rigid plug would obstruct pilus passage through the secretin channel, whereas a slightly mobile one could restrict influx yet be displaced when the IM complex docks, allowing subsequent T4P assembly. This interpretation also explains why the plug does not support coordinate building at the present map quality. Taken together, our data support a model in which Slk proteins seal the PilQ secretin channel upon its assembly but are displaced upon IM complex docking to permit T4P assembly. When IM complex assembly or docking is delayed, Slk proteins would be retained in the PilQ channel, preventing toxic compound influx and maintaining the OM permeability barrier.

SlkAB homologs are predominantly found in gamma-proteobacteria and not widely conserved among bacterial species that have the T4PS or other secretin-containing virulence systems (Supplementary Fig. 14), but we speculate that different types of plug proteins for secretin

channels may exist among bacteria that lack SlkAB homologs. In many transenvelope systems with OM secretin channels, assembly of secretin complexes occurs independently of the IM complex assembly[10,27,31–34]. Thus, defective assembly of the IM complex or improper alignment between the OM and IM complexes in these systems might also cause a breach in the permeability barrier function of the OM. Proteins that help seal the secretin channels may therefore exist in other secretin-dependent virulence systems as well. In this regard, it is noteworthy that other important secretin-interacting proteins are also divergent in sequence. For example, pilotins, which deliver secretins to the OM and/or aid in secretin assembly, belong to several groups of proteins that are unrelated in their sequence and structure even though they serve a similar function[35,36]. We thus suspect that proteins preventing diffusion through secretin channels might also be diverse among systems with secretin channels.

Because we identified the OM permeability defect of the *slk* mutant with macrolides that are lipophilic, we initially suspected that the T4P secretin channel might preferentially facilitate the diffusion of hydrophobic drugs. However, hydrophobicity did not seem to be a general property of the compounds that permeate through the secretin channel. Instead, this channel increased susceptibility of *P. aeruginosa* to several classes of drugs with different chemical properties. Thus, although the loss of Slk protein function combined with defects in T4P assembly clearly creates a PilQ-dependent OM permeability defect, the precise chemical features that promote permeation through the secretin channel remain to be determined. Understanding these and other determinants of OM permeation will be critical for the development of future antibiotic therapies effective against Gram-negative pathogens.

OM secretin channels are essential components of many virulence systems and thus have been considered as attractive targets for development of antivirulence drugs[10,37]. Our discovery that the PilQ channel functions as a pore for drug diffusion in the absence of Slk proteins and IM

complex docking indicates that secretin channels can also be exploited as conduits to facilitate drug delivery into Gram-negative pathogens. Thus, understanding how secretin-dependent systems prevent diffusion of toxic compounds through secretin channels is a promising avenue for developing effective strategies to broaden the spectrum of approved antibiotics to include activity against Gram-negative infections.

Methods

Strains, media, and strain manipulation

Strains and plasmids used in this study are listed in Supplementary Tables 4,5. Detailed procedures for strain and plasmid construction are also provided in the Supplementary Information. Bacterial cells were grown in either LB [1% tryptone, 0.5% yeast extract, 0.5% NaCl], Vogel-Bonner minimal medium (VBMM) [3.42 g/L trisodium citrate dihydrate, 2 g/L citric acid, 10 g/L K_2HPO_4, 3.5 g/L $NaNHPO_4$-$4H_2O$, pH7, 1 mM $MgSO_4$, 0.1 mM $CaCl_2$], or minimal M9 medium supplemented with glucose [6 g/L Na_2HPO_4 anhydrous, 3 g/L KH_2PO_4, 0.5 g/L NaCl, 1 g/L NH_4Cl, 0.2% glucose, 2 mM $MgSO_4$, 0.1 mM $CaCl_2$].

Allelic replacement in *P. aeruginosa*

Suicide plasmids for gene knockout or fusion at native genetic loci were introduced into *P. aeruginosa* by conjugation with the *E. coli* donor strain Sm10(λpir). Clones carrying integrated plasmid via homologous recombination were selected on VBMM agar supplemented with 30 μg/mL gentamicin; for strains with OM barrier defects, the gentamicin concentration was lowered to 10 μg/mL to prevent suppressor mutants. Counterselection to isolate double-crossover recombinants was performed on LB agar supplemented with 5% sucrose.

Electroporation for gene expression

Gene expression plasmids were introduced by electroporation using electrocompetent cells prepared in 0.3 M sucrose solution [38]. For chromosomal integration of a gene expression cassette at the Tn7 attachment site, recipient strains were co-electroporated with a suicide plasmid carrying the cassette flanked by Tn7 end sequences and pTNS3 [*bla oriR6K tnsABCD*] that expresses Tn7 transposase. Transformants were selected on LB agar supplemented with 30 μg/mL gentamicin; for strains with OM barrier defects, 10 μg/mL gentamicin was used.

Generation of the transposon insertion library

P. aeruginosa strains were mutagenized using the mariner transposon delivery vector pBTK30 [39]. The plasmid was transferred to *P. aeruginosa* strains via mating with the donor strain SM10(*λpir*) carrying pBTK30. Mating was performed on LB agar at 37 °C for 1hours, and transconjugants were selected on VBMM agar supplemented with 30 µg/mL gentamicin. Colonies were harvested by resuspension in VBMM broth with 10% glycerol and stored at -80 °C.

Transposon sequencing

A transposon mutant library of PAO1 was thawed and incubated in LB for roughly two doublings. The resuscitated mutant library culture was diluted in LB either lacking or containing 10 µg/mL erythromycin and incubated for 10 doublings to a final OD_{600} of 0.5 at 37 °C. After the incubation, the cells were pelleted and frozen. Genomic DNA from each cell pellet was extracted, fragmented, and poly-C tailed as previously described [40]. The transposon-chromosome junctions in the resulting DNA were amplified by using Easy-A enzyme (Agilent Technologies). The primers used were the poly-C tail-specific primer 5'-GTGACTGGAGTTCAGACGTGTGCTCTTCCGATCTGGGGGGGGGGGGGGGG-3' and the transposon-specific primer 5'-GGTTCTGGACCAGTTGCGTGAG-3'. The transposon-chromosome junctions were further amplified in a second, nested PCR with the primers that add sequencing barcodes to each mutant library, NEBNext Multiplex Oligos for Illumina (NEB), and the transposon-specific primer 5'-AATGATACGGCGACCACCGAGATCTACACTCTTTGTTTTCTGGAAGGCGAGCATCGTTTG-3'. The final PCR products were quantified, and equal amounts of each barcoded library were mixed. The pooled sequencing library was run on a 2% agarose gel, and DNA fragments ranging from 200 and 500 bp were excised and purified using QIAquick Gel Extraction Kit

(Qiagen). The resulting library was sequenced using a MiSeq reagent kit V3 (150-cycle) (Illumina) with the custom primer 5'-CTAGAGACCGGGGACTTATCAGCCAACCTGTTA-3'. Sequencing reads were trimmed using trimmomatic [41] to remove adaptor sequences, and mapped to chromosomal TA dinucleotides (mariner insertion sites) on the *P. aeruginosa* PAO1 genome (NC_002516) using bowtie 1.0.0 [42]. Differences in the total number of reads at any given TA site between untreated and erythromycin-treated samples were determined using a Mann-Whitney U test. Transposon insertion profiles were visualized using the Sanger Artemis Genome Browser and Annotation tool.

qRT-PCR

To compare *slkA* and *slkB* expression levels, overnight cultures were diluted in LB to an OD_{600} of 0.04 and incubated at 37 °C to an OD_{600} of 0.3~0.4. Then, RNA was extracted and reverse transcribed. Real-time PCRs were performed using the following primer pairs: *rpoA*-F (5′-GAAGTCCCTGACCGAAATCAA-3′) and *rpoA*-R (5′-GTGGCCTTGTCGTCTTTCTTA-3′); *slkA*-F (5′-CCGACCAATACCGTAGGAATC-3′) and *slkA*-R (5′-GTTGAAGGTGCCGTTGTTG-3′); and *slkB*-F (5′-CGGTGTTCCCGTTGAAGAA-3′) and *slkB*-R (5′-CACTCGATGCAGGTGGAAG-3′). Reactions were run on a Quantstudio 1 (Applied Biosystems) with an initial denaturation step at 95 °C for 15 min, followed by 45 cycles at 95 °C for 10 s, 60 °C for 15 s, and 72 °C for 30 s. Experiments were performed in triplicates, and relative gene expression levels were calculated using the $2^{-\Delta\Delta Ct}$ method with normalization to *rpoA*.

Suppressor selection

To select for suppressors of the erythromycin susceptibility phenotype of OKP7 (PAO1 Δ*slkAB*), the strain was mutagenized by random insertion of a mariner-based transposon from pBTK30. The mutant library was spread on LB agar supplemented with 50 μg/mL erythromycin to select for mutants that can suppress the OM permeability defect. The transposon insertion sites of the

suppressors were determined by arbitrarily primed PCR. The first round was performed with a primer pair 5'-GGCCACGCGTCGACTAGTACNNNNNNNNNNGATAT-3' and 5'-GGTTCTGGACCAGTTGCGTGAG-3'. The second, nested PCR was performed with 5'-GGCCACGCGTCGACTAGTAC-3' and 5'- CGAACCGAACAGGCTTATGTCAATTCG-3' to increase specificity and sensitivity. The resulting PCR products were sequenced with the primer 5'-CGAACCGAACAGGCTTATGTCAATTCG-3' that anneal to the transposon sequence to identify the transposon-chromosome junctions.

Antibiotic susceptibility testing – agar diffusion assay

Freshly saturated cultures were adjusted to OD_{600} = 2.0, and 125 µL of each culture was mixed with 5 mL molten H-top soft agar (1% tryptone, 0.8% NaCl, 0.7% agar) and spread onto LB agar. MIC Test Strips (Liofilchem) were then applied to the solidified soft agar containing bacterial cells. Alternatively, antibiotics were serially diluted, and 5 µL of each dilution was spotted onto the soft agar. The plates were incubated for 24 hours at 37 °C before being photographed.

Twitching motility assay

To examine T4P-mediated twitching motility, a single colony from a freshly streaked LB agar plate was picked with a toothpick and stab-inoculated through LB agar (1% agar) to the bottom of a polystyrene dish. After incubation for 48 hours at 30 °C, the LB agar was removed and the cells attached to the dish were stained with 1% crystal violet for 5 min. The dish was then rinsed with water to remove excess stain, and the stained zone was photographed after air drying.

Microscopic image acquisition and analysis

Growth conditions prior to microscopy are described in the figure legends. Prior to imaging, cells were immobilized on 2% agarose pads containing 1X M9 salts and covered with #1.5

coverslips. Micrographs were obtained using a Leica DM2500 LED microscope equipped with a Leica DFC7000 GT camera, Fluo Illuminator LRF 4/22, HC PL APO 100x/1.40 Oil Ph3 objective lens, and Leica Las X acquisition software. Images in the red channel were obtained using N2.1 filter cube. Automated cell segmentation and identification as well as measurements of fluorescence signal at the single cell level were carried out using Oufti[43]. For demographs, custom-written MATLAB code was used to arrange cells from top to bottom according to their length as previously described[44].

Immunoblotting

Cells in 2 mL cultures with an OD_{600} of approximately 0.5 were harvested by centrifugation. The cell pellets were resuspended in 0.2 mL of 1× Laemmli sample solution and heated at 95 °C for 10 min. Then, proteins were separated by SDS-PAGE and transferred onto a PVDF membrane. SlkA- and SlkB-mScarlet levels and RpoA levels were probed with a rabbit polyclonal anti-mScarlet antibody (custom-generated by AbClon) at a dilution of 1:2,000, and a mouse monoclonal anti-RpoA antibody (clone 4RA2, BioLegend, Cat: 663104, Lot: B252705) at a dilution of 1:40,000. Anti-mouse IgG, HRP-linked antibody (Cell Signaling Technology, Cat: 7076S, Lot: 33) and goat anti-rabbit IgG polyclonal antibody (HRP conjugate) (Enzo Life Sciences, Cat: ADI-SAB-300-J, Lot: 08151814) were both used at a dilution of 1:20,000 for detection of mScarlet and RpoA signals.

Phylogenetic tree generation

The cladogram was generated from the bacterial reference phylogenetic tree (release v226) in the Genome Taxonomy Database (GTDB), which comprises 136,646 bacterial species clusters[45]. To improve readability, the tree was collapsed to the genus level using the ETE3 Python package (v3.1.3)[46] and subsequently visualized with Dendroscope software (v3.8.10)[47]. Amino acid sequences of PA5122 and PA5123 were queried against the NCBI non-redundant

protein sequence database using BLASTP[48]. Proteins showing significant similarity (*E*-value≤1.0×10^{-6}) to either PA5122 or PA5123 were considered homologs and annotated on the cladogram.

Membrane solubilization and purification

Pseudomonas aeruginosa strains OKP181(attTn7::pKHT105), OKP181(attTn7::pOKP170), OKP181(attTn7::pOKP171) (PilQ-only, PilQ-SlkA, and PilQ-SlkB expressing strain, respectively) were grown in LB with gentamicin at 37 °C with shaking. Overnight cultures were diluted 1:100 into 200 mL LB with gentamicin and grown at 37 °C to OD_{600} = 1.0. Cells were transferred into 4 L LB and incubated for 18 hours at 37 °C.

Cell pellets were harvested at 6,000 × g for 20 min at 4 °C, resuspended, and lysed in 50 mM Tris–HCl pH 8.0, 20% (w/v) sucrose, 3% (w/v) Anzergent 3-14 (Anatrace, U.S.A), lysozyme 0.5 mg/mL, and protease inhibitors. Lysis and solubilization proceeded for 20 hours at 4 °C with gentle stirring. Insoluble material was removed at 50,000 × g for 1 hours at 4 °C. The supernatant was incubated with Ni^{2+}–NTA resin pre-equilibrated in lysis buffer. Resin was washed with 50, 100, and 200 mM imidazole and eluted with 1 M imidazole. Eluates were dialyzed for 10 hours at 4 °C, concentrated with a 100 kDa MWCO concentrator, and polished by size-exclusion chromatography (Superose 6 Increase 10/300 GL) in 50 mM Tris–HCl pH 8.0, 150 mM NaCl, 0.02% (w/v) Anzergent 3-14. Fractions corresponding to PilQ–SlkA, PilQ–SlkB, or PilQ-only were pooled and used immediately for vitrification.

Cryo-EM grid preparation

Quantifoil R1.2/1.3 200-mesh copper grids with a continuous 2nm/ultra-thin carbon film were negatively glow-discharged at 5 mA for 5 s. Purified protein (0.03 mg/mL) was applied to each grid in three sequential 4 µL aliquots, with multiple rounds of sample application and blotting.

The grids were then vitrified in liquid ethane using a Vitrobot Mark IV (Thermo Fisher Scientific, USA) at 4 °C and 100% relative humidity.

Cryo-EM data acquisition

Data were acquired at the Institute for Basic Science on a Krios G4 (Thermo Fisher Scientific, USA) operated at 300 kV and equipped with a BioQuantum energy filter (20 eV slit) and a K3 direct electron detector (Gatan, USA). Automated acquisition in EPU (Thermo Fisher Scientific, USA) was performed in electron-counting, super-resolution mode at a nominal magnification of 53,000x (calibrated pixel size 0.81 Å). Movies were recorded as 40-frame stacks over 2.0 s, delivering a total exposure of 53.1 e^{-}/Å^2, with target defocus values from −0.7 to −1.8 µm.

Image processing

Image processing was performed in cryoSPARC v4.5.1.[49] Movies were aligned and dose-weighted using Patch Motion Correction, and defocus were estimated using Patch CTF. For SlkA, manual and template picks were used to train a Topaz model[50]. The model was then fine-tuned on SlkB and Empty datasets and used for automated particle picking. Extracted particles underwent multiple rounds of 2D classification, followed by ab initio 3D reconstruction and heterogeneous classification. Final particle sets contained 63,311 (SlkA), 111,983 (SlkB), and 18,241 (Empty) as summarized in Supplementary Fig. 11. Homogeneous refinements were performed with C14 symmetry and with C1 symmetry. Gold-standard procedures were used throughout. Global map resolutions at FSC 0.143 were 2.68 Å and 3.06 Å for SlkA (EMD-66449 (C14) and EMD 66446 (C1)), 2.45 Å and 2.85 Å for SlkB (EMD-66448 (C14) and EMD 66445 (C1)), and 3.02 Å and 4.35 Å for Empty (EMD-66447 (C14) and EMD 66444 (C1)), as reported in Supplementary Figs. 11,13. For focused refinement, C1-focused runs used soft masks

encompassing the central lumen and gate region. Masks were generated from the C1 consensus map with a cosine soft edge and were applied to SlkA, SlkB, and PilQ-only datasets. To test whether the plug exhibits local symmetry, we generated a particle-subtracted stack retaining the luminal plug (non-luminal signal removed) and performed focused refinements with a lumen-restricted mask, imposing various symmetries (C2, C3, C5, C7, C9, and C11) about the channel axis. None of these settings improved density features or local resolution. For subclass analysis, particles contributing to the C1 consensus were subjected to additional heterogeneous classification in C1, and subclass volumes were refined independently under the same masking protocol. Local resolution was estimated in cryoSPARC and maps were automatically sharpened (Supplementary Fig. 13). To assess conformational heterogeneity, 3D variability analysis (3DVA)[51] as performed in cryoSPARC on the same particle stack used above, running the analysis in C1 with a soft mask confined to the lumen and gate-proximal region.

Map interpretation and model building

Maps were visualized in UCSF ChimeraX[52] and Chimera[53]. Initial models for the PilQ barrel and periplasmic region were auto-traced with ModelAngelo[54], manually adjusted in Coot[55], and refined by real-space refinement in Phenix[56] with secondary-structure and geometry restraints. Over-fitting was monitored by refining against one half-map and evaluating model–map FSC against the other (Supplementary Table 2,3). For the exterior component, the OM protein identified by proteomics (PA0359) was modeled *de novo* directly into the ring-like outer-membrane α-helical density and refined. A single phosphatidylethanolamine lipid was modeled at the interface between the exterior protein and PilQ (Supplementary Fig. 15). Views of a previous PilQ map (EMD-21153)[57] were reproduced under matched display settings (Supplementary Fig.16). To register our single-particle maps to the *in situ* reference, PilQ–SlkA and PilQ–SlkB volumes were rigid-body fit to the *P. aeruginosa* T4P subtomogram average

(EMD-43432)[30] in ChimeraX using fitmap with lumen-centered masks. Orthoslices and merged overlays were generated in IMOD (3dmod) Slicer[58] with matched slice thickness and contrast across datasets. Cross-correlations were computed across a range of mask dilations and low-pass cutoffs. For overlay visualization only, the C1 SPA map was Gaussian low-pass filtered to match the effective resolution of the subtomogram average. Overlays for the Δ*pilC* dataset were prepared using the same settings (Fig. 5b,c).

Proteomics (label-free TIMS–TOF)

For proteomic analysis, PilQ–SlkA, PilQ–SlkB, and PilQ-only complexes were prepared following the same purification procedure described above, except that cultures were scaled up to 12 L to obtain protein at a concentration of at least 0.1 mg/mL prior to mass spectrometry. PilQ complexes were analyzed by label-free LC-MS on a timsTOF platform (TimsTOF flex MALDI-2, Bruker, Germany). MS1 peak areas were integrated and normalized by total-ion current. Database searching used a *Pseudomonas aeruginosa* PAO1 reference proteome with 1% FDR at PSM and protein levels. Acquisition and data processing followed established timsTOF PASEF workflows[59] . Protein IDs and quantitative values are provided in Supplementary Table 1. The mass spectrometry proteomics data have been deposited to the ProteomeXchange Consortium via the PRIDE[60] partner repository with the dataset identifier PXD077666.

Data availability

The data supporting the findings of this study are available within the paper and its Supplementary Information files. Cryo-EM density maps generated in this study have been deposited in the Electron Microscopy Data Bank (EMDB) under the following accession codes: EMD-66447 [https://www.ebi.ac.uk/pdbe/entry/emdb/EMD-66447] (PilQ, C14); EMD-66449 [https://www.ebi.ac.uk/pdbe/entry/emdb/EMD-66449] (PilQ–SlkA, C14); EMD-66448 [https://www.ebi.ac.uk/pdbe/entry/emdb/EMD-66448] (PilQ–SlkB, C14); EMD-66444 [https://www.ebi.ac.uk/pdbe/entry/emdb/EMD-66444] (PilQ, C1); EMD-66446 [https://www.ebi.ac.uk/pdbe/entry/emdb/EMD-66446] (PilQ–SlkA, C1); and EMD-66445 [https://www.ebi.ac.uk/pdbe/entry/emdb/EMD-66445] (PilQ–SlkB, C1). Atomic coordinates have been deposited in the Protein Data Bank (PDB) under accession codes 9X0W [https://doi.org/10.2210/pdb9x0w/pdb] (PilQ in C14), 9X0Y [https://doi.org/10.2210/pdb9x0y/pdb] (PilQ fitted/refined into the SlkA-bound map), and 9X0X [https://doi.org/10.2210/pdb9x0x/pdb] (PilQ fitted/refined into the SlkB-bound map). Coordinates for the exterior outer-membrane side component (PA0359) are included in all three PDB entries. No atomic coordinates are provided for the Slk luminal densities. Label-free LC–MS/MS raw data and search results for PilQ-only, PilQ–SlkA, and PilQ–SlkB preparations have been deposited to the ProteomeXchange Consortium via the PRIDE partner repository under accession PXD077666 [http://proteomecentral.proteomexchange.org/cgi/GetDataset?ID=PXD077666]. Previously deposited data referenced in this study: EMD-43432 [https://www.ebi.ac.uk/pdbe/entry/emdb/EMD-43432] (subtomogram average of the *P. aeruginosa* T4P system from a *pilY1* mutant) and EMD-21153 [https://www.ebi.ac.uk/pdbe/entry/emdb/EMD-21153] (PAO1 wild-type PilQ map). The *P. aeruginosa* PAO1 reference genome used for read mapping is available at NC_002516 [https://www.ncbi.nlm.nih.gov/nuccore/NC_002516]. Source data are provided with this paper.

Code availability

Code used to collapse the bacterial phylogenetic tree to the genus level is publicly available at https://github.com/SKKU-ChoeLab/Collapse_GTDB_Phylotree under the GNU General Public License v3.0 (GPLv3).

References

1. Nikaido, H. Molecular basis of bacterial outer membrane permeability revisited. *Microbiol. Mol. Biol. Rev.* **67**, 593–656 (2003).

2. Delcour, A. H. Outer membrane permeability and antibiotic resistance. *Biochim. Biophys. Acta Proteins Proteom.* **1794**, 808–816 (2009).

3. Silver, L. L. Challenges of antibacterial discovery. *Clin. Microbiol. Rev.* **24**, 71–109 (2011).

4. Raetz, C. R. H. & Whitfield, C. Lipopolysaccharide endotoxins. *Biochemistry* **71**, 635–700 (2002).

5. Krishnamoorthy, G. *et al.* Synergy between active efflux and outer membrane diffusion defines rules of antibiotic permeation into Gram-negative bacteria. *mBio* **8**, e01172-17 (2017).

6. Li, X.-Z., Plésiat, P. & Nikaido, H. The challenge of efflux-mediated antibiotic resistance in Gram-negative bacteria. *Clin. Microbiol. Rev.* **28**, 337–418 (2015).

7. Pagès, J.-M., James, C. E. & Winterhalter, M. The porin and the permeating antibiotic: a selective diffusion barrier in Gram-negative bacteria. *Nat. Rev. Microbiol.* **6**, 893–903 (2008).

8. Prajapati, J. D., Kleinekathöfer, U. & Winterhalter, M. How to enter a bacterium: bacterial porins and the permeation of antibiotics. *Chem. Rev.* **121**, 5158–5192 (2021).

9. Majewski, D. D., Worrall, L. J. & Strynadka, N. C. Secretins revealed: structural insights into the giant gated outer membrane portals of bacteria. *Curr. Opin. Struct. Biol.* **51**, 61–72 (2018).

10. Korotkov, K. V., Gonen, T. & Hol, W. G. J. Secretins: dynamic channels for protein transport across membranes. *Trends Biochem. Sci.* **36**, 433–443 (2011).

11. Weaver, S. J. *et al.* Cryo-EM structure of the type IVa pilus secretin required for natural competence in *Vibrio cholerae*. *Nat. Commun.* **11**, 5080 (2020).

12. Hu, J. *et al.* Cryo-EM analysis of the T3S injectisome reveals the structure of the needle and open secretin. *Nat. Commun.* **9**, 3840 (2018).

13. D'Imprima, E. *et al.* Cryo-EM structure of the bifunctional secretin complex of *Thermus thermophilus*. *eLife* **6**, e30483 (2017).

14. Naskar, S., Hohl, M., Tassinari, M. & Low, H. H. The structure and mechanism of the bacterial type II secretion system. *Mol. Microbiol.* **115**, 412–424 (2021).

15. Disconzi, E. *et al.* Bacterial secretins form constitutively open pores akin to general porins. *J. Bacteriol.* **196**, 121–128 (2014).

16. Li, X.-Z., Nikaido, H. & Poole, K. Role of mexA-mexB-oprM in antibiotic efflux in *Pseudomonas aeruginosa*. *Antimicrob. Agents Chemother.* **39**, 1948–1953 (1995).

17. Tsutsumi, K. *et al.* Structures of the wild-type MexAB–OprM tripartite pump reveal its complex formation and drug efflux mechanism. *Nat. Commun.* **10**, 1520 (2019).

18. Ayers, M. *et al.* PilM/N/O/P proteins form an inner membrane complex that affects the stability of the *Pseudomonas aeruginosa* type IV pilus secretin. *J. Mol. Biol.* **394**, 128–142 (2009).

19. Koo, J. *et al.* PilF is an outer membrane lipoprotein required for multimerization and localization of the *Pseudomonas aeruginosa* type IV pilus secretin. *J. Bacteriol.* **190**, 6961–6969 (2008).

20. Wehbi, H. *et al.* The peptidoglycan-binding protein FimV promotes assembly of the *Pseudomonas aeruginosa* type IV pilus secretin. *J. Bacteriol.* **193**, 540–550 (2011).

21. Klockgether, J. *et al.* Genome diversity of *Pseudomonas aeruginosa* PAO1 laboratory strains. *J. Bacteriol.* **192**, 1113–1121 (2009).

22. Sidorenko, J., Jatsenko, T. & Kivisaar, M. Ongoing evolution of *Pseudomonas aeruginosa* PAO1 sublines complicates studies of DNA damage repair and tolerance. *Mutat. Res. Fundam. Mol. Mech. Mutagen.* **797**, 26–37 (2017).

23. Chandler, C. E. *et al.* Genomic and phenotypic diversity among ten laboratory isolates of *Pseudomonas aeruginosa* PAO1. *J. Bacteriol.* **201**, e00001-19 (2019).

24. Takhar, H. K., Kemp, K., Kim, M., Howell, P. L. & Burrows, L. L. The platform protein is essential for type IV pilus biogenesis. *J. Biol. Chem.* **288**, 9721–9728 (2013).

25. Burrows, L. L. *Pseudomonas aeruginosa* twitching motility: type IV pili in action. *Annu. Rev. Microbiol.* **66**, 493–520 (2012).

26. McCallum, M., Burrows, L. L. & Howell, P. L. The dynamic structures of the type IV pilus. *Microbiol. Spectr.* **7**, e00001-19 (2019).

27. Carter, T. *et al.* The type IVa pilus machinery is recruited to sites of future cell division. *mBio* **8**, e02103-16 (2017).

28. Chang, Y.-W. *et al.* Architecture of the type IVa pilus machine. *Science* **351**, aad2001 (2016).

29. Treuner-Lange, A. *et al.* PilY1 and minor pilins form a complex priming the type IVa pilus in *Myxococcus xanthus*. *Nat. Commun.* **11**, 5054 (2020).

30. Guo, S. *et al.* PilY1 regulates the dynamic architecture of the type IV pilus machine in *Pseudomonas aeruginosa*. *Nat. Commun.* **15**, 9382 (2024).

31. Diepold, A. & Wagner, S. Assembly of the bacterial type III secretion machinery. *FEMS Microbiol. Rev.* **38**, 802–822 (2014).

32. Friedrich, C., Bulyha, I. & Søgaard-Andersen, L. Outside-in assembly pathway of the type IV pilus system in *Myxococcus xanthus*. *J. Bacteriol.* **196**, 378–390 (2014).

33. Douzi, B., Filloux, A. & Voulhoux, R. On the path to uncover the bacterial type II secretion system. *Philos. Trans. R. Soc. Lond. B Biol. Sci.* **367**, 1059–1072 (2012).

34. Thomassin, J., Moreno, J. S., Guilvout, I., Nhieu, G. T. V. & Francetic, O. The trans-envelope architecture and function of the type II secretion system: new insights raising new questions. *Mol. Microbiol.* **105**, 211–226 (2017).

35. Silva, Y. R. de O., Contreras-Martel, C., Macheboeuf, P. & Dessen, A. Bacterial secretins: mechanisms of assembly and membrane targeting. *Protein Sci.* **29**, 893–904 (2020).

36. Koo, J., Burrows, L. L. & Howell, P. L. Decoding the roles of pilotins and accessory proteins in secretin escort services. *FEMS Microbiol. Lett.* **328**, 1–12 (2012).

37. Baron, C. Antivirulence drugs to target bacterial secretion systems. *Curr. Opin. Microbiol.* **13**, 100–105 (2010).

38. Choi, K.-H. & Schweizer, H. P. mini-Tn7 insertion in bacteria with single attTn7 sites: example *Pseudomonas aeruginosa*. *Nat. Protoc.* **1**, 153–161 (2006).

39. Goodman, A. L. *et al.* A signaling network reciprocally regulates genes associated with acute infection and chronic persistence in *Pseudomonas aeruginosa*. *Dev. Cell* **7**, 745–754 (2004).

40. Lai, G. C., Cho, H. & Bernhardt, T. G. The mecillinam resistome reveals a role for peptidoglycan endopeptidases in stimulating cell wall synthesis in *Escherichia coli*. *PLoS Genet.* **13**, e1006934 (2017).

41. Bolger, A. M., Lohse, M. & Usadel, B. Trimmomatic: a flexible trimmer for Illumina sequence data. *Bioinformatics* **30**, 2114–2120 (2014).

42. Langmead, B., Trapnell, C., Pop, M. & Salzberg, S. L. Ultrafast and memory-efficient alignment of short DNA sequences to the human genome. *Genome Biol.* **10**, R25 (2009).

43. Paintdakhi, A. *et al.* Oufti: an integrated software package for high-accuracy, high-throughput quantitative microscopy analysis. *Mol. Microbiol.* **99**, 767–777 (2016).

44. Sher, J. W., Lim, H. C. & Bernhardt, T. G. Global phenotypic profiling identifies a conserved actinobacterial cofactor for a bifunctional PBP-type cell wall synthase. *eLife* **9**, e54761 (2020).

45. Parks, D. H. *et al.* GTDB: an ongoing census of bacterial and archaeal diversity through a phylogenetically consistent, rank-normalized and complete genome-based taxonomy. *Nucleic Acids Res.* **50**, D785–D794 (2021).

46. Huerta-Cepas, J., Serra, F. & Bork, P. ETE 3: reconstruction, analysis, and visualization of phylogenomic data. *Mol. Biol. Evol.* **33**, 1635–1638 (2016).

47. Huson, D. H. & Scornavacca, C. Dendroscope 3: an interactive tool for rooted phylogenetic trees and networks. *Syst. Biol.* **61**, 1061–1067 (2012).

48. Camacho, C. *et al.* BLAST+: architecture and applications. *BMC Bioinformatics* **10**, 421 (2009).

49. Punjani, A., Rubinstein, J. L., Fleet, D. J. & Brubaker, M. A. cryoSPARC: algorithms for rapid unsupervised cryo-EM structure determination. *Nat. Methods* **14**, 290–296 (2017).

50. Bepler, T. *et al.* Positive-unlabeled convolutional neural networks for particle picking in cryo-electron micrographs. *Nat. Methods* **16**, 1153–1160 (2019).

51. Punjani, A. & Fleet, D. J. 3D variability analysis: resolving continuous flexibility and discrete heterogeneity from single-particle cryo-EM. *J. Struct. Biol.* **213**, 107702 (2021).

52. Pettersen, E. F. *et al.* UCSF ChimeraX: structure visualization for researchers, educators, and developers. *Protein Sci.* **30**, 70–82 (2021).

53. Pettersen, E. F. *et al.* UCSF Chimera—a visualization system for exploratory research and analysis. *J. Comput. Chem.* **25**, 1605–1612 (2004).

54. Jamali, K. *et al.* Automated model building and protein identification in cryo-EM maps. *Nature* **628**, 450–457 (2024).

55. Emsley, P., Lohkamp, B., Scott, W. G. & Cowtan, K. Features and development of Coot. *Acta Crystallogr. Sect. D Biol. Crystallogr.* **66**, 486–501 (2010).

56. Afonine, P. V. *et al.* Real-space refinement in PHENIX for cryo-EM and crystallography. *Acta Crystallogr. Sect. D Struct. Biol.* **74**, 531–544 (2018).

57. McCallum, M., Tammam, S., Rubinstein, J. L., Burrows, L. L. & Howell, P. L. Cryo-EM map of *Pseudomonas aeruginosa* PilQ enables structural characterization of TsaP. *Structure* **29**, 457–466.e4 (2021).

58. Kremer, J. R., Mastronarde, D. N. & McIntosh, J. R. Computer visualization of three-dimensional image data using IMOD. *J. Struct. Biol.* **116**, 71–76 (1996).

59. Meier, F. *et al.* Online parallel accumulation–serial fragmentation (PASEF) with a novel trapped ion mobility mass spectrometer. *Mol. Cell. Proteomics* **17**, 2545–2559 (2018).

60. Perez-Riverol, Y. *et al.* The PRIDE database at 20 years: 2025 update. *Nucleic Acids Res.* **53**, D543–D553 (2025).

Acknowledgements

We thank members of the Cho and Chung labs for their helpful suggestions. We also thank the staff of the cryo-EM facility at the Institute for Basic Science (IBS, Daejeon, Republic of Korea) for assistance with cryo-EM data collection.

Funding

This work was supported by the National Research Foundation of Korea (NRF) (RS-2022-NR067344, RS-2023-00228746, and RS-2025-00522505 to H.C.; RS-2022-NR071689 to J.M.C.) and by a National Research Facilities and Equipment Center grant funded by the Ministry of Education (RS-2025-02310063 to J.M.C.). Use of the cryo-EM facilities of the NEXUS consortium was supported by NRF grant RS-2024-00440289 (to J.M.C.). This work was also supported by the Catholic University of Korea Research Fund 2021 (to J.M.C.).

Author Contributions Statement

O.H.K., B.K., and S.P. performed genetic and cell biology experiments. Y.L., B.R., and J.M.C. performed cryo-EM sample preparation, data collection, image processing, and structural modeling. J.W.S., F.L., S.-H.C., D.C., Y.-H.C., J.-F.C., and T.G.B. provided technical support for Tn-seq and cell biology experiments. Y.Y. and M.D.O. provided conceptual and technical advice on cryo-EM experiments. O.H.K., Y.L., B.R., J.M.C., and H.C. conceived the experiments and wrote the manuscript. All authors reviewed and edited the manuscript.

Competing Interests Statement

The authors declare no competing interests.

Figure Legends

Fig. 1 | SlkA and SlkB play an important role in maintaining the envelope permeability barrier. a, Scheme for identifying mutations that cause an envelope barrier defect. Mutants that have a defect in the permeability barrier function become susceptible to erythromycin treatment and mutations that cause erythromycin susceptibility are identified by a Tn-seq approach. **b**, Transposon insertion profiles for *PA5122-PA5123* (*slkAB*) and *oprM* loci. Lines above the locus map represent transposon insertion sites and the height of the lines reflects the number of sequencing reads at each site. Regions with significantly fewer reads in the erythromycin-treated sample compared with the untreated sample are indicated with red dotted lines. **c**, Spot dilution assay for PAO1 (WT), OKP5 (*ΔslkA*), OKP6 (*ΔslkB*), and OKP7 (*ΔslkAB*) strains on LB agar only or supplemented with 50 μg/mL erythromycin. The strains grown overnight normalized to OD_{600} = 2 were serially diluted 10-fold and spotted onto LB agar lacking or containing 50 μg/mL erythromycin. The plates were incubated at 37 °C and photographed after 20 hours. **d**, Spot dilution assay for PAO1 harboring pJN105 (empty vector) and OKP7 (*ΔslkAB*) strains harboring pJN105, pOKP17 (*slkA*), or pOKP18 (*slkB*) on LB agar supplemented with 50 μg/mL erythromycin. **e**, Comparison of the sensitivity of *ΔslkAB* and *ΔoprM* strains to various antibiotics. Cells of the PAO1, OKP7 (*ΔslkAB*), and OKP62 (*ΔoprM*) strains were mixed with molten soft agar and overlaid on LB plates. Test strips impregnated with indicated antibiotics in a concentration gradient were then placed on the lawn of cells and the plates were imaged after incubation for 24 hours at 37 °C. All experiments were repeated at least two or three times, and representative results are shown. Source data are provided as a Source Data file for Fig. 1b–e.

Fig. 2 | Assembly of the PilQ secretin complex of the T4PS causes the envelope barrier defect of the *ΔslkAB* strain. a, A diagram of the transposon insertion sites of the suppressors isolated from the selection of the OKP7(*ΔslkAB*) strain on LB agar containing 50 μg/mL

erythromycin. The triangles above the locus map represent the insertion for which the direction of transcription in the gentamicin resistance cassette of the transposon is in the same orientation as the disrupted gene; the triangles below, opposite direction. **b**, PAO1, OKP7(*ΔslkAB*), OKP15 (*ΔslkAB ΔpilQ*), and OKP50 (*ΔslkAB ΔpilMNOPQ*) strains harboring a chromosomally integrated expression construct attTn7::pOKP121 [$P_{toplac\text{-}uv5}$::*pilQ*] or an empty vector control attTn7::pKHT105 were grown in LB containing 1mM IPTG, serially diluted, and spotted onto indicated LB agar supplemented with 1mM IPTG to keep inducing *pilQ* expression. PAO1 and OKP7 (*ΔslkAB*) strains were also grown and spotted for comparison of growth phenotype. **c**, Sensitivity of PAO1, OKP7 (*ΔslkAB*), OKP14 (*ΔpilQ*), OKP15 (*ΔslkAB ΔpilQ*) strains to macrolide antibiotics was compared using indicated antibiotic test strips as in Fig. 1e. Source data are provided as a Source Data file for Fig. 2b–c.

Fig. 3 | Effect of type IV pili mutations on the drug diffusion through the PilQ complex in the *ΔslkAB* strain. a, Comparison of twitching motility among PAO1, $PAO1^{tw+}$, PA14, PAK, and their *ΔslkAB* derivatives. A single colony of each strain was stab-inoculated through LB agar to the polystyrene dish. After incubation for 48 hours at 30 °C, LB agar was removed, and the cells attached to the polystyrene dish were stained with crystal violet and photographed. Twitching zone areas were quantified using ImageJ, and analyzed by two-way ANOVA in GraphPad Prism 8.4.3 (n = 12; ns, not significant). **b**, The diagram at the top shows a frameshift mutation in *pilC* of the PAO1 strain used for the Tn-seq and initial characterization. The twitching-defective PAO1 strain and its *ΔslkAB* derivative (OKP7) harboring pJN105 (empty vector) or pOKP139 expressing *pilC* from the twitching-proficient strain were tested for twitching motility on the polystyrene dish. **c**, The same strains were grown overnight in LB supplemented with 10 μg/mL gentamicin, serially diluted in LB, spotted onto LB agar lacking or containing 50 μg/mL

erythromycin, and imaged after incubation for 20 hours at 37 °C. **d-f**, Spot dilution assays to test the effect of T4P gene mutations on the drug permeation through the PilQ secretin complex of the *ΔslkAB* strain. Mutations in the platform (*pilC*), the pilus shaft (*pilA* and *pilY1*), and alignment complex (*pilMNOP*) genes were introduced in the PAO1^{tw+} strain and its *ΔslkAB* and *ΔslkAB ΔpilQ* derivatives. The resulting strains were grown in LB, serially diluted, spotted onto LB agar lacking or containing 50 μg/mL erythromycin, and photographed. The inactivated T4P gene products in each spot dilution assay, *pilC* for (**d**), *pilA* or *pilY1* for (**e**), and *pilMNOP* for (**f**), are indicated with dotted lines and fainter color in the cartoons on the right. Minor pilins are drawn as an unlabeled rod between PilY1 and PilA, and PilBTU is omitted for simplicity. (**f**) For testing the effect of alignment complex inactivation, *pilQ* was expressed from an ectopic locus as in Fig. 2b to avoid polar effects on *pilQ* expression by *pilMNOP* mutation. The LB and LB agar contained 1 mM IPTG to induce *pilQ* expression. Source data are provided as a Source Data file for Fig. 3a–f.

Fig. 4 | PilQ-dependent polar localization of SlkA and its enhancement upon inactivation of the T4P platform PilC. a, A PAO1^{tw+} derivative that express *slkA-mScarlet* from its native locus (OKP59) and its *ΔpilQ*, *ΔpilC*, and *ΔpilC ΔpilQ* derivatives (OKP60, OKP61, and OKP120) were grown overnight in LB. SlkA-mScarlet was partially functional and its expression level was not altered by pilC or pilQ mutations (Supplementary Fig. 9,10) The overnight cultures were diluted 1:100 in M9-glucose (0.2%) medium, grown to exponential phase (OD_{600} = 0.2~0.3), and imaged on 2% agarose pads containing 1X M9 salts. Shown on top of each panel are representative fluorescent images showing the localization of SlkA-mScarlet in each strain. Bar equals 3 μm. Below the micrographs are demographs that reflect SlkA-mScarlet localization throughout a population of 500 cells arranged according to cell length. Single-cell fluorescence

quantification was performed using Oufti [43]. **b**, The mean SlkA-mScarlet signal intensity profile per unit length was calculated for the 500 single-cells of each strain shown in (**a**). Each plot displays the mean signal every 0.0648 microns for 11 points, spanning from the outermost cell tips inward. The cell pole is defined by the yellow highlighted region corresponding to the outermost 0.324 microns. **c**, Quantification of SlkA-mScarlet signal at the poles. Shown are mean and standard deviation of the SlkA-mScarlet fluorescent signal intensity at the cell poles, defined in (**b**), for each of the indicated strains. Source data are provided as a Source Data file.

Fig. 5 | Slk proteins plug the PilQ secretin lumen and align with the central gate-proximal density *in situ*. a, Single-particle cryo-EM density maps (C1, semi-transparent) with rigid fits of a PilQ atomic model built against the C14 reconstruction**.** C1 maps are shown to visualize the asymmetric luminal plug, which is attenuated by C14 symmetry averaging. A PilQ model built against the C14 map is rigidly fitted into each C1 volume for reference. Three states are shown: PilQ–SlkA (magenta), PilQ–SlkB (green) and PilQ-only (blue). The outer membrane (OM) plane and periplasm (PP) are indicated. PilQ-only presents an unobstructed conduit, whereas Slk-bound complexes contain a continuous luminal mass extending from the vestibule toward the periplasm. In PilQ–SlkB the plug sits deeper and engages a broader inner-wall footprint than in PilQ–SlkA. Axial and radial dimensions are annotated. **b**, Rigid alignment of the *in vitro* C1 maps (PilQ–SlkA) to the published *in situ* subtomogram average of the *P. aeruginosa* T4P system (EMD-43432). Left, *in vitro*; middle, *in situ*; right, merged. The Slk-derived luminal mass overlays the central gate-proximal density observed in cells. Red outlines indicate the gate region and the luminal mass. **c**, Segmented and fitted views of the *in vitro* complex, the *in situ* average and the merged volume. The *in vitro* panel uses the C1 PilQ–SlkA map Gaussian-filtered to match the effective resolution of the Cryo-ET average. A magenta PilQ atomic model (built against the

C14 map and rigidly fitted into each volume) is overlaid to register the barrel and gate, highlighting the one-to-one correspondence between the luminal plug and the central *in situ* density at the gate. **d**, Working model. Left to right: PilQ without Slk forms a conduit that permits entry of compounds (blue circles). SlkA or SlkB (red) engage the channel upon its assembly to plug the pore and prevent influx. Docking of the IM complex and subsequent pilus assembly displaces Slk proteins, enabling pilus transit through the PilQ channel and preventing influx. Major components of the IM complex are indicated for context. Cartoons are not to scale. Accession codes: EMD-66446 (PilQ–SlkA, C1), EMD-66445 (PilQ–SlkB, C1), EMD-66444 (PilQ, C1); EMD-66449 (PilQ–SlkA, C14), EMD-66448 (PilQ–SlkB, C14), EMD-66447 (PilQ, C14). PDB 9X0W, 9X0Y, 9X0X (Coordinates for the exterior OM-side component (PA0359) are included in all three PDB entries but are not displayed in panels a and c; only PilQ coordinates are rendered in this figure).

Editorial Summary

The assembly of type IV pili in Gram-negative bacteria involves the formation of secretin channels in the outer membrane. Here, the authors identify two periplasmic proteins that seal the secretin channel during pilus assembly, thus preventing loss of the outer-membrane permeability barrier.

Peer Review Information: *Nature Communications* thanks the anonymous reviewers for their contribution to the peer review of this work. A peer review file is available.

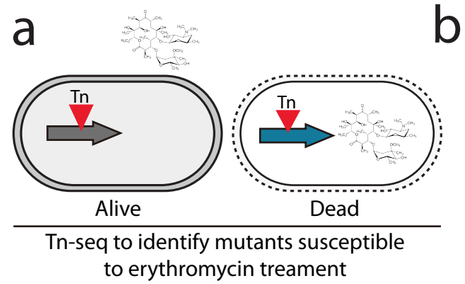
a
Tn
Tn
Alive
Dead
Tn-seq to identify mutants susceptible
to erythromycin treament

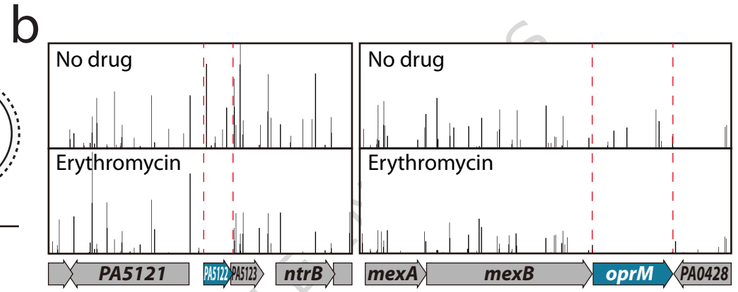
b
No drug
Erythromycin
No drug
Erythromycin
PA5121
PA5122
PA5123
ntrB
mexA
mexB
oprM
PA0428

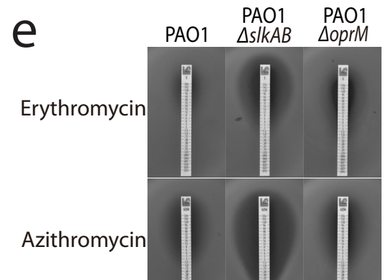
e
PAO1
PAO1 ΔslkAB
PAO1 ΔoprM
Erythromycin
Azithromycin

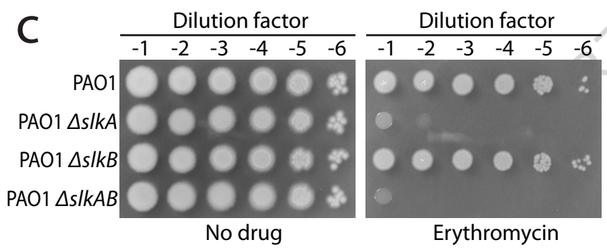
c
Dilution factor
-1 -2 -3 -4 -5 -6
Dilution factor
-1 -2 -3 -4 -5 -6
PAO1
PAO1 ΔslkA
PAO1 ΔslkB
PAO1 ΔslkAB
No drug
Erythromycin

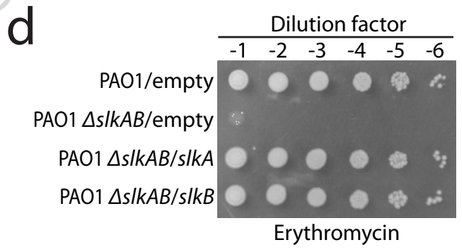
d
Dilution factor
-1 -2 -3 -4 -5 -6
PAO1/empty
PAO1 ΔslkAB/empty
PAO1 ΔslkAB/slkA
PAO1 ΔslkAB/slkB
Erythromycin

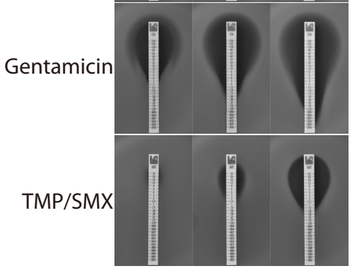
Gentamicin
TMP/SMX

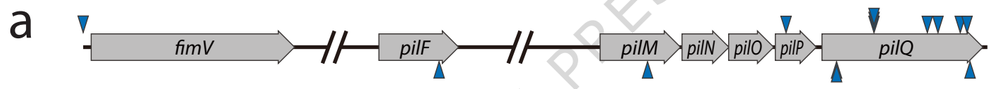
a
fimV
pilF
pilM
pilN
pilO
pilP
pilQ

b
Dilution factor
-1 -2 -3 -4 -5 -6 -1 -2 -3 -4 -5 -6
PAO1(Ptoplac-uvs::empty)
PAO1(Ptoplac-uvs::pilQ)
PAO1 ΔslkAB(Ptoplac-uvs::empty)
PAO1 ΔslkAB ΔpilQ(Ptoplac-uvs::empty)
PAO1 ΔslkAB ΔpilQ(Ptoplac-uvs::pilQ)
PAO1 ΔslkAB ΔpilMNOPQ(Ptoplac-uvs::empty)
PAO1 ΔslkAB ΔpilMNOPQ(Ptoplac-uvs::pilQ)
LB-IPTG
LB-IPTG-Erythromycin

c
PAO1
PAO1 ΔslkAB
PAO1 ΔpilQ
PAO1 ΔslkAB ΔpilQ
Erythromycin
Azithromycin

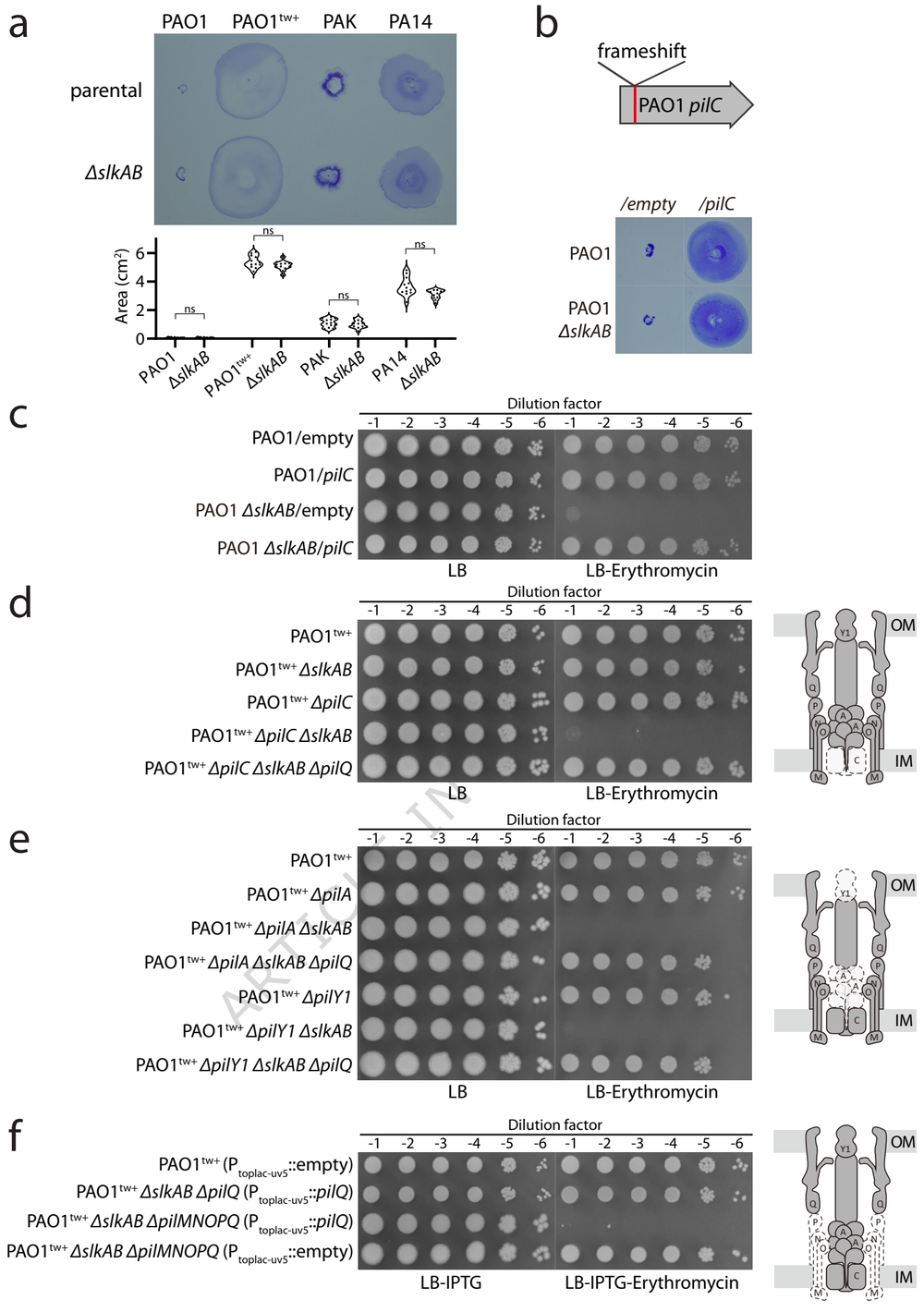

a

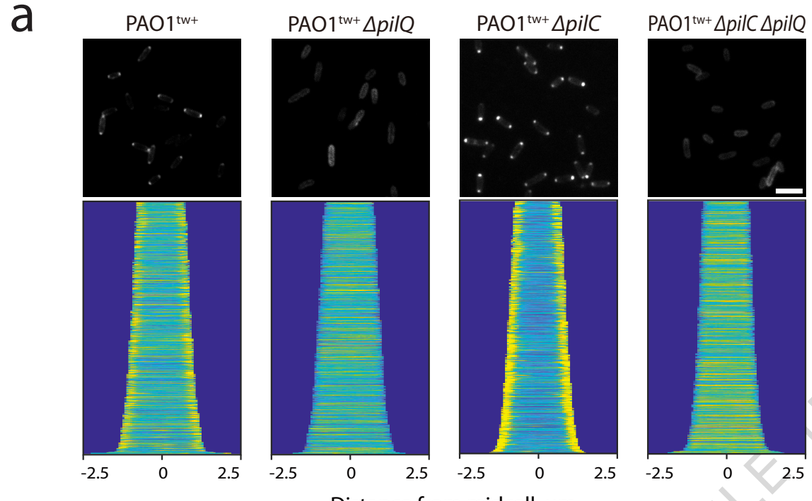

b

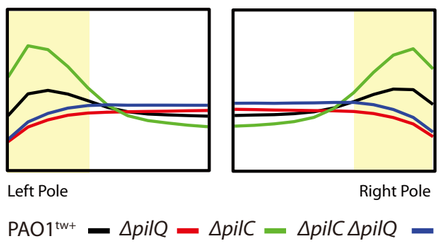

c

Strain	Total Average Signal at Poles
PAO1^{tw+}	0.554 +/- 0.005
ΔpilQ	0.369 +/- 0.002
ΔpilC	0.786 +/- 0.016
ΔpilC ΔpilQ	0.418 +/- 0.003

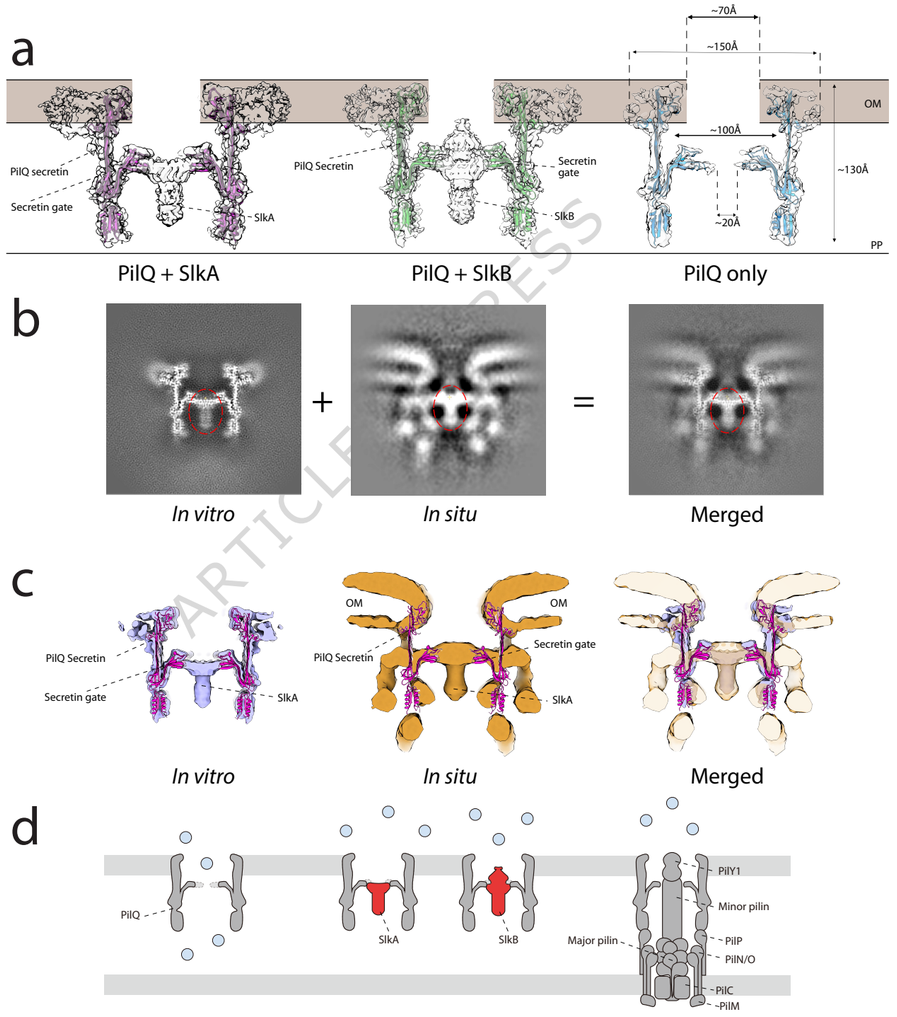
a
~70Å
~150Å
OM
~100Å
~130Å
~20Å
PP
PilQ secretin
Secretin gate
SlkA
PilQ Secretin
Secretin gate
SlkB
PilQ + SlkA
PilQ + SlkB
PilQ only
b
+
=
In vitro
In situ
Merged
c
PilQ Secretin
Secretin gate
SlkA
OM
OM
PilQ Secretin
Secretin gate
SlkA
In vitro
In situ
Merged
d
PilQ
SlkA
SlkB
PilY1
Minor pilin
PilP
PilN/O
Major pilin
PilC
PilM